Civil and Environmental Engineering Faculty Publications

Civil and Environmental Engineering

1-23-2023

Antimony nanobelt asymmetric membranes for sodium ion battery

Logan Williams

Jake DiCesare

Olivia Sheppard

Congrui Grace Jin

Xiaobo Chen

See next page for additional authors

Authors

Logan Williams, Jake DiCesare, Olivia Sheppard, Congrui Grace Jin, Xiaobo Chen, and Ji Wu

PAPER

Antimony nanobelt asymmetric membranes for sodium ion battery

View the article online for updates and enhancements.

Antimony nanobelt asymmetric membranes for sodium ion battery

Logan Williams[1,4]**, Jake DiCesare**[1,4]**, Olivia Sheppard**[1,4]**, Congrui Jin**[2,*] **,**
Xiaobo Chen[3] **and Ji Wu**[1,*]

[1] Department of Chemistry and Biochemistry, Georgia Southern University, 250 Forest Drive, Statesboro, GA 30460, United States of America
[2] Department of Civil and Environmental Engineering, University of Nebraska-Lincoln, 362Q Whittier, 2200 Vine St., Lincoln, NE, 68583, United States of America
[3] Materials Science and Engineering Program, Binghamton University, New York, NY 13902, United States of America

E-mail: jwu@georgiasouthern.edu and cjin5@unl.edu

CrossMark

Abstract

In this study, composite asymmetric membranes containing antimony (Sb) nanobelts are prepared via a straightforward phase inversion method in combination with post-pyrolysis treatment. Sb nanobelt asymmetric membranes demonstrate improved cyclability and specific capacity as the alloy anode of sodium ion battery compared to Sb nanobelt thin films without asymmetric porous structure. The unique structure can effectively accommodate the large volume expansion of Sb-based alloy anodes, prohibit the loss of fractured active materials, and aid in the formation of stable artificial solid electrolyte interphases as evidenced by an outstanding capacity retention of ~98% in 130 cycles at 60 mA g^{-1}. A specific capacity of ~600 mAh g^{-1} is obtained at 15 mA g^{-1} (1/40C). When the current density is increased to 240 mA g^{-1}, ~80% capacity can be maintained (~480 mAh g^{-1}). The relations among phase inversion conditions, structures, compositions, and resultant electrochemical properties are revealed through comprehensive characterization.

Supplementary material for this article is available online

Keywords: antimony nanobelt, asymmetric membrane, dip coating, alloy anode, sodium ion battery

(Some figures may appear in colour only in the online journal)

1. Introduction

Lithium-ion batteries (LIBs) currently dominate the ever-growing electrochemical energy storage (EES) market as driven by the insatiable demand from mobile electronics, portable power tools, electrical vehicles, as well as static energy storage systems [1–3]. The scarcity of lithium element in Earth's crust, however, necessitates more sustainable battery materials, especially for large scale applications. Additionally, lithium salts are usually produced from underground reservoirs or mines, thus requiring costly acquisition processes, and raising significant

environmental concerns [4, 5]. On the other hand, the abundance of sodium is nearly three orders of magnitude higher than that of lithium. Thereby, transition from LIBs to sodium-ion batteries (SIBs) may provide a massive relief on the global environment and improve the affordability of EES systems [6]. However, Na$^+$ has a much larger ionic radius compared to Li$^+$, so the conventional LIB anode, graphite is unable to store Na$^+$ reversibly [7, 8]. Researchers worldwide have investigated other carbon-based materials for SIB anode with impressive advancements, such as expanded graphite, hard carbon, and carbon nanotubes with capacities of ~284, 320, and 215 mAh g^{-1} respectively [8, 9]. Of considerable note, elemental antimony exhibits an impressive theoretical capacity of 660 mA

g^{-1}, by means of alloying/dealloying reaction mechanism shown below [10–12]:

$$Sb + Na^+ + e^- \rightarrow NaSb,$$

$$NaSb + 2Na^+ + 2e^- \rightarrow Na_3Sb.$$
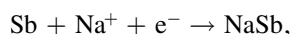
Sadly, a high capacity is intrinsically associated with a large volume change during sodiation/desodiation, thereby resulting in electrode pulverization, unstable solid electrolyte interphase (SEI), and rapid capacity loss. Quite a few strategies have been proposed to accommodate the large volume change of antimony-based alloy anodes, most of which focus on nano-structuring, compositing, alloying, as well as developing new binders and electrolyte additives [10, 13–15]. Recently, asymmetric membrane structure has been adopted by our laboratory for the first time to alleviate the severe volume expansion of high-capacity anodes in LIBs, such as Si, Ge and Sn nano/micron particles [16–21]. In this study, antimony nanobelts embedded in carbonaceous asymmetric membranes are synthesized, characterized and employed as the alloy anode material for high capacity/performance SIBs. It is hypothesized that the two-dimensional morphology of nanobelts together with the asymmetric porous structure of the membrane is expected to have a synergetic impact on the electrochemical performance of Sb-based alloy anodes since nanobelts can provide additional advantages such as continuous framework, strong mechanical strength, and shortened diffusion length. The novelty of this research is the incorporation of two-dimensional nanobelts into asymmetric membranes for high performance sodium-ion battery for the first time.

2. Methods

2.1. Synthesis of antimony oxide nanobelts

Antimony oxide (Sb_2O_3) nanobelts (NBs) were synthesized using an adapted method from the literature [22]. To describe it briefly, 2.4 g Sb powder (BEANTOWN CHEMICAL, ~200 mesh, 99.5% trace metals basis), 150 mmol ethyl diamine (VWR), 0.8 g polyvinylpyrrolidone (Sigma Aldrich), and 1.5 l deionized water were used to create a homogenous slurry that was stirred for 1 h at 60 °C, followed by sitting at room temperature over the weekend. The white precipitate was then collected by vacuum filtration and washed thoroughly using de-ionized water and absolute ethanol to obtain Sb_2O_3 NBs.

2.2. Fabrication of antimony nanobelt asymmetric membrane (Sb NB PAN)

2.4 g Sb_2O_3 NBs were mixed with 0.15 g carbon black (CB TIMCAL SUPER C45 with a surface area of 45 m^2 g^{-1}), 0.50 g polyacrylonitrile (PAN) (Mn = 150 000; Pfaltz & Bauer) dissolved in 10 ml N-methyl-2-pyrrolidone (NMP) (Sigma Aldrich, >99.5%) using a probe sonicator at 15 W power. The resultant slurry was then coated, using a doctor blade, onto a silicon wafer with a thickness setting of 200 μm and submerged into deionized water for 10 min for the phase

inversion process to complete. In the next step, the polymeric asymmetric membrane containing Sb_2O_3 NBs underwent pyrolysis at 500 °C for 4 h under the protection of helium gas (99.9999%, Airgas He UHP300) with a flow rate of 100 sccm to produce Sb nanobelt asymmetric membrane labeled Sb NB PAN. This process was carried out using a Lindber/Blue MTM 1100 °C tube furnace whose temperature was ramped at a rate of ~60 °C min^{-1}. Noteworthy, when the concentration of PAN was more than 10 wt%, the slurry was too viscous to make smooth coatings. If the concentration of PAN was less than 3 wt%, the slurry was too fluidic to coat. In other words, there is a narrow window for the concentration of PAN used to make Sb asymmetric membranes. CB was mainly used as a filler to maintain the porous structure during the pyrolysis process, without which the pores can collapse as confirmed by our previous studies [20]. However, when the concentration of CB was too high, the slurry became too viscous and unsuitable for smooth coatings.

2.3. Fabrication of dip-coated antimony nanobelt asymmetric membrane (dip-coated Sb NB PAN)

First, a slurry made of 0.11 g CB, 0.38 g PAN and 10 ml NMP was created using a probe sonicator at 15 W power. Next, Sb NB PAN was submerged in the slurry, slowly pulled out from the slurry, and immediately placed in deionized water. Lastly, the sample was pyrolyzed for 2 h at 500 °C to create a porous carbon coating on its surface and labeled dip-coated Sb NB PAN.

2.4. Fabrication of antimony powder asymmetric membrane (Sb PAN)

2.0 g of antimony micron-powder (BeanTown Chemical Inc.) were added to a solution composed of 0.20 g CB, 0.65 g PAN, and 10 ml NMP. The slurry was subject to the same procedure as described above for Sb NB PAN: sonication, phase inversion, and pyrolysis. Notably, the concentration of Sb in Sb PAN membrane is close to that of dip-coated Sb NB PAN (~80 wt%; see S3).

2.5. Characterization methods

Morphological, compositional, and structural characterization was accomplished using a field emission scanning electron microscope (JEOL JSM-7600F) attached with transmission electron detector (TED) and energy dispersive x-ray analyzer (EDS). Raman spectra were collected using a Thermo Scientific DXR SmartRaman spectrometer with 0.4–1.0 mW, 532 nm laser, ×10 objective lens, and 30–120 s integration time. A thermogravimetric analyzer (TGA, TA Instruments Q50 TGA) was used to quantify the concentration of the active materials using nitrogen (Airgas) as the purging gas at a flow rate of 20 ml min^{-1}. The oven temperature during TGA analysis was ramped at 10 °C min^{-1} until 120 °C and held for 10 min to remove all water present in the sample. The temperature was then ramped at 10 °C min^{-1} until 500 °C and held for 30 min. Powder x-ray diffractometry (PXRD, PANanalytical Empyrean) was performed using a Cu K$_\alpha$ radiation (λ = 1.540 598 Å) from 10° to

80° (two theta) at a step rate of $0.1° \text{ s}^{-1}$ for 32 times with acceleration voltage and current of 40 kV and 40 mA, respectively. X-ray photoelectron spectroscopy (XPS) system was employed to measure the binding energy of Sb core-level electrons using a monochromatic Al K_α x-ray, an x-ray spot size of 400 μm, a pass energy of 50 eV, an energy step size of 0.1 eV. The specific surface areas of asymmetric membranes were measured by Micromeritics ASAP 2020 Surface Area and Porosity analyzer at UNL in combination with Brunauer–Emmett–Teller (BET) method after the samples were degassed at 50 μTorr and 300 °C for 30 min. High resolution transmission electron microscopy (HRTEM) characterization was performed using a FEI Talos F200X operated at an accelerating voltage of 200 kV.

2.6. Electrode preparation and electrochemical analysis

Approximately 1–2 mg of Sb containing asymmetric membranes were glued onto aluminum current collectors with diameter and thickness of 15 mm and 11 μm, respectively. The glue was composed of 0.15 g carbon black, 0.10 g carboxymethyl cellulose (ACROS ORGANICS, average M.W. 9000) binder, and 3 ml deionized water. Two control electrodes, Sb powder and Sb NB thin films were also prepared to investigate the impact of asymmetric membrane structure on cycling stability and capacity. 200 μm thin films were made from a slurry consisting of 0.21 g CB, 0.07 g polyvinylidene fluoride (PVDF; MTI Corp.), 3 ml NMP and 1.0 g Sb micronsize powder or 1.2 g Sb_2O_3 nanobelts, in which the concentration of active materials was calculated to be ∼80 wt%, close to that in dip-coated Sb NB PAN. Electrodes were then dried at 80 °C for 24 h under vacuum before they were assembled into 2032-type coin cells. 1 M $NaClO_4$ (ACROS ORGANICS, Sodium perchlorate, ACS reagent, anhydrous) dissolved in a mixture of 47.5% v/v propylene carbonate (PC), 47.5% ethylene carbonate (EC) and 5% fluoroethylene carbonate (FEC) (Alfa Aesar, propylene carbonate, 99%, ACROS ORGANICS, ethylene carbonate >99%, and Alfa Aesar, fluoroethylene carbonate, 98%) was used as the electrolyte. Sodium metal (Sigma Aldrich) and glass fiber membrane (Whatman, GLASS MICROFIBER FILTERS) were employed as the counter electrode and membrane separator, respectively. All assembly was performed in an Ar-filled glove box (LCPW, LC Technology Solutions, Inc.), keeping moisture and oxygen concentrations below 1ppm. Galvanostatic cycling tests were conducted on all samples using a multi-channel Potentiostat/EIS (BIO-LOGIC VMP3). Two formation cycles were allowed to proceed at a current density of 15 mA g^{-1}, aiding in the formation of a stable SEI layer on the electrode. Rate performance tests were carried out at 15, 60, 240 and then back to 60 mA g^{-1} for both charging and discharging within a voltage window of 0.01–2.00 V (versus Na/Na$^+$). For cyclic voltammetry testing, the voltage was scanned periodically from 0.01 to 2.00 V at different rates. A frequency range of 0.1 Hz–1.00 MHz was applied with an AC perturbation of 10 mV during the electrochemical impedance spectroscopy (EIS) measurements.

3. Results and discussion

3.1. Fabrication of antimony nanobelt asymmetric membranes

Sb nanobelts have several advantages over micron-sized particles for SIB alloy anode: (1) the thin thickness of NB (<100 nm) allows for faster charging/discharging, due to a shortened diffusion length; (2) the strong mechanical strength of NB avoids extensive electrode pulverization; (3) the two-dimensional (2D) structure of NB with a large length to width ratio improves the electrical contact between active materials and conductive additives, especially for SIB alloy anodes with significant changes in electrode volume during charging/discharging. Moreover, asymmetric membrane structure can effectively stabilize LIB alloy anodes as confirmed by our prior works [16, 19, 20]. Therefore, 2D nanobelt is introduced into asymmetric membrane structure, aiming to maximize the cyclability and capacity of Sb-based alloy anodes for SIBs via a synergic effect as illustrated in figure 1.

3.2. Characterization

Scanning electron microscope (SEM) was employed to investigate the morphology of Sb powder, Sb_2O_3 NB and Sb asymmetric membranes. As purchased Sb powder has irregular shapes with sizes up to ∼80 μm (figure 2(a)). The width of NBs ranges from ∼200 to 800 nm, and the typical length of NBs is more than 100 μm (figure 2(b)). The large length to width ratio (up to ×1000) is critical to maintaining a close contact between NB and CB, especially when NB may be partially fractured or structurally changed during repeated sodiation/de-sodiation. The thickness of Sb_2O_3 nanobelts is ∼20 nm (figures 2(c), (d)), which can significantly shorten diffusion time for sodium ions. Figures 2(e) and (f) show that the sizes of Sb particles have been reduced from up to 80 μm to less than 10 μm in Sb PAN membrane, due to the strong probe sonication that may break up the particles. The 2D morphology of NB can be retained after Sb_2O_3 is reduced to elemental Sb in Sb NB PAN membrane (figures 2(g) and (h)). Notably, the length and width of Sb NB in Sb NB PAN are smaller than those in Sb_2O_3 NB because of the probe sonication process and reduction reaction that occurred during the high temperature pyrolysis treatment. The asymmetric porous structure of Sb PAN and Sb NB PAN membranes was verified by the differential surface views shown in S1 and S2. EDS elemental mappings and SEM images confirmed the formation of thin, porous carbon on the top surface of dip-coated Sb NB PAN, through which sodium ions can transport freely without being significantly hindered (figure 3). Additionally, the carbon coating can increase the conductivity of the membrane electrode, further prohibit the loss of fractured active materials and aid in the formation of artificial SEI layers, thus enhancing the electrochemical performance of the membrane electrode as evident by the following electrochemical data.

Next, the chemical composition of the materials was investigated using Raman spectroscopy, powder x-ray diffraction (PXRD) and x-ray photoelectron spectroscopy
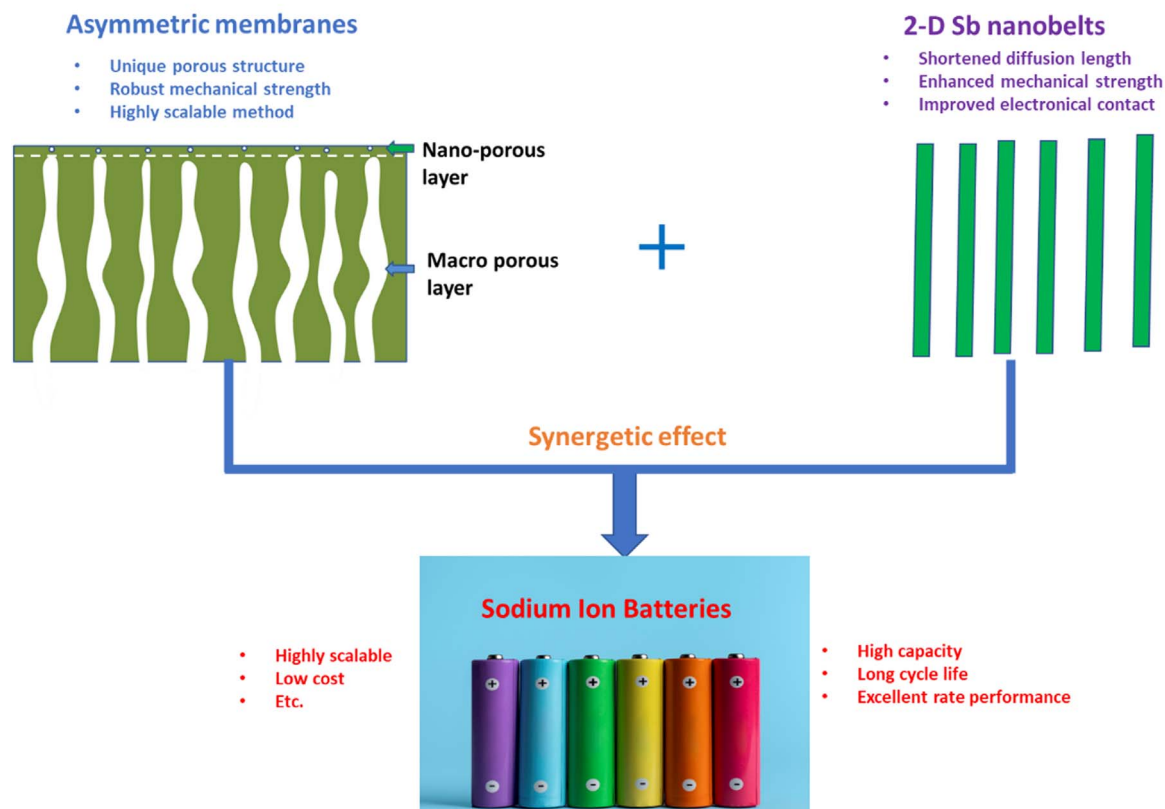
Figure 1. Schematic illustration of the membrane fabrication process that utilizes the synergetic effect of asymmetric membrane and 2D nanobelt for high capacity/performance sodium ion battery alloy anode.

(XPS). The peaks centered at 142, 190, 220, 298, 443, 505, 590 and 685 cm^{-1} in the Raman spectrum of NB are consistent with orthorhombic Sb$_2$O$_3$, in which 590 and 685 cm^{-1} Raman shifts correspond to asymmetric (v_{as}) and symmetric (v_s) stretching modes while the peaks centered at 443 and 505 cm^{-1} are due to the asymmetric (δ_{as}) and symmetric (δ_s) bending modes of SbO$_3$ pyramids (figure 4(a)) [22]. NB exhibited characteristic PXRD patterns of orthorhombic Sb$_2$O$_3$ at 19.3°, 28.6° and 36.4° (2θ), corresponding to (110), (040) and (200) crystallographic orientations, respectively (PDF#43–1071; figure 4(b)). However, the intensity of (200) peak from Sb$_2$O$_3$ NB is much stronger compared to Sb$_2$O$_3$ reference from database, indicating the NB has a preferential growth along the crystallographic orientation, and being consistent with literature report [22]. This, in combination with Raman data, confirms the synthesized nanobelts consist of pure orthorhombic Sb$_2$O$_3$. The PXRD patterns indicate that Sb PAN, Sb NB PAN and dip-coated Sb NB PAN are composed of amorphous carbon and elemental antimony as confirmed by the characteristic patterns of rhombohedral Sb at 28.6°, 40.1° and 41.9° (2θ) from (012), (104) and (110) crystal orientations, respectively (PDF#35–0732), identical to the patterns of Sb powder and Sb reference from database (figure 4(b)). It is believed that the reduction of Sb$_2$O$_3$ during the pyrolysis process is responsible for the production of elemental antimony in Sb NB PAN and dip-coated Sb NB

PAN as represented by the following chemical reaction:

$$Sb_2O_3 + 3C \xrightarrow{\Delta} 2Sb + 3CO \uparrow.$$
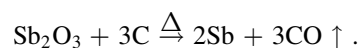
XPS spectra of Sb PAN, Sb NB PAN and dip-coated Sb NB PAN (figure 4(c)) have two intense peaks at ∼529 and ∼538 eV as can be attributed to 3d$_{3/2}$ and 3d$_{5/2}$ of Sb (0), respectively. The two satellite peaks at ∼531 and ∼540 eV from oxidized Sb (III) are stronger in Sb NB PAN and dip-coated Sb NB PAN than in Sb PAN. It is because nanomaterials tend to be oxidized more extensively than their bulk counterparts, considering nanomaterials have much larger specific surface areas. Recall that Sb NB PAN and dip-coated Sb NB PAN were made from nanobelts, whereas micronsized Sb powder was used to fabricate Sb PAN.

HRTEM was utilized to obtain the crystallographic information of the samples. As shown figure 5(b), a d-spacing of 0.26 nm was observed from Sb$_2$O$_3$ NBs, which originates from the (200) lattice plane in orthorhombic Sb$_2$O$_3$. D-spacings of 0.31 and 0.23 nm were identified in the NBs of Sb NB PAN and dip-coated Sb NB PAN membranes, corresponding to (012) and (104) lattice planes of elemental antimony, respectively (figures 5(c) and (d)). Carbon materials in all samples seem to be amorphous. Noteworthy, Sb NBs were found to be much smaller than Sb$_2$O$_3$ NBs, due to the reasons discussed above. Furthermore, the membranes must be crushed and dispersed in acetone using a strong probe sonicator for HRTEM imaging.
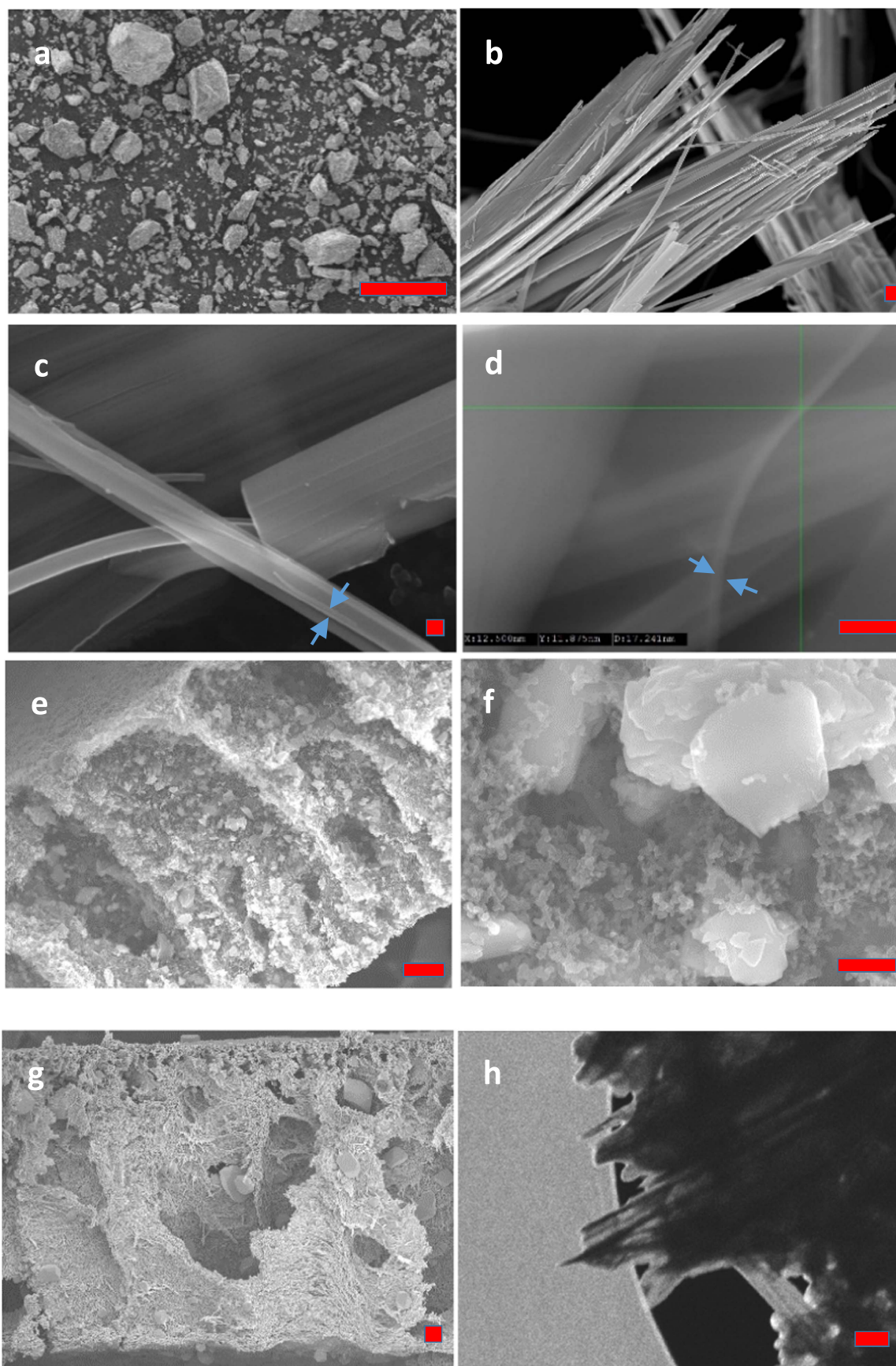
Figure 2. SEM images of (a) Sb powder; (b) Sb nanobelts; (c) and (d) cross-sectional view of individual Sb$_2$O$_3$ nanobelt; (e) and (f) cross-sectional view of Sb PAN membrane at different magnifications; (g) cross-sectional view of Sb NB PAN membrane; (h) TEM image of Sb *nanobelt* embedded in Sb NB PAN membrane. Scale bars are 100 μm, 1 μm, 100 nm,100 nm, 10 μm, 1 μm, 10 μm and 100 nm from (a) to (h).
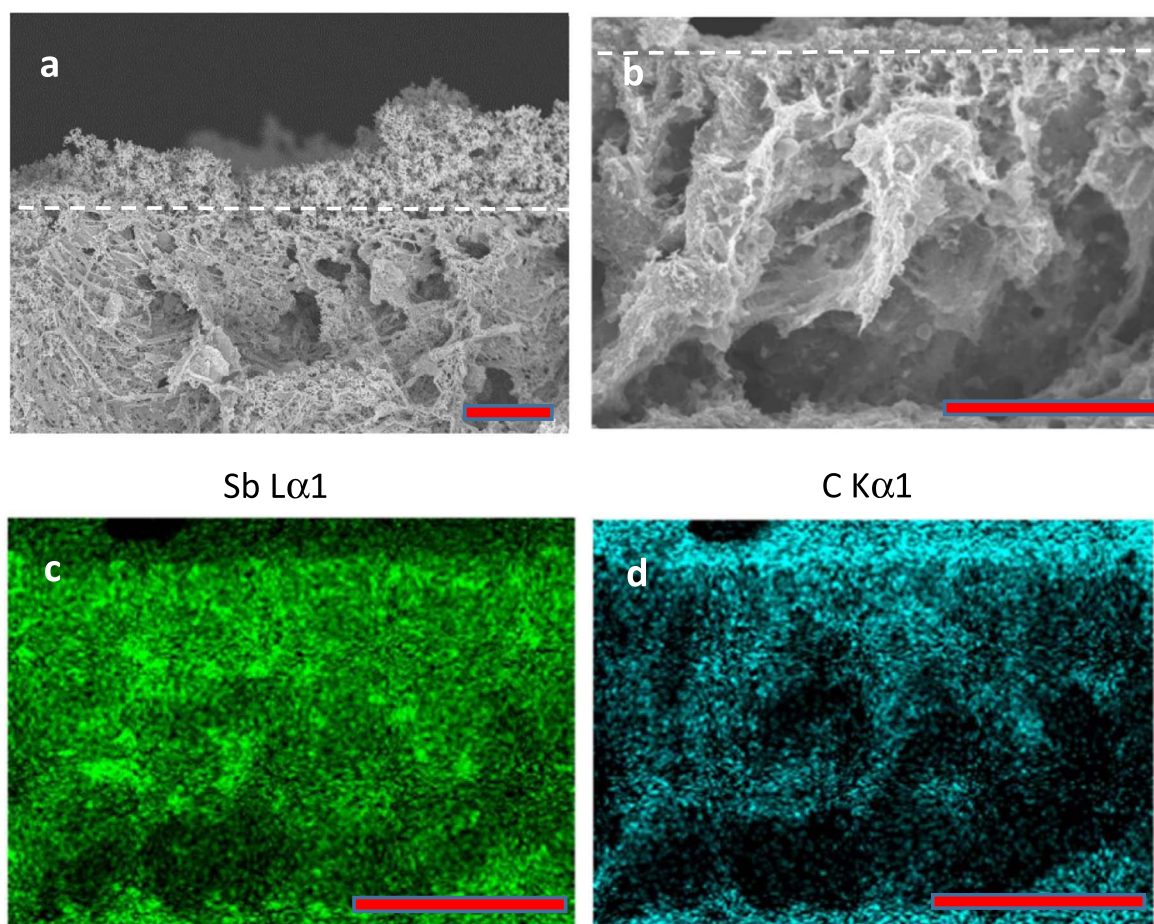
Figure 3. (a) and (b) are cross-sectional SEM images of dip-coated Sb NB PAN membrane at different magnifications; (c) and (d) are elemental mappings of Sb and C using energy-dispersive x-ray spectroscopy (EDS), corresponding to the SEM image shown in (b). Scale bars are 10 μm, 100 μm, 100 μm and 100 μm from (a) to (d).

3.3. Electrochemical analysis

Sb PAN membrane was the first sample to undergo electro-chemical testing as SIB anode. The membrane electrode demonstrated a high initial capacity loss (ICL) of 25.5% (figure 6 and table 1), which can be attributed to the irreversible decomposition of electrolyte during the formation of SEI layer on the surface of fractured Sb powder. Although merely 34.1% capacity was retained after 50 cycles at 60 mA g^{-1}, the retention is still better than the thin film electrode made of Sb powder ($\sim$100% capacity loss), suggesting that the asymmetric membrane structure can significantly enhance the cyclability of micron-sized Sb particles as initially hypothesized (table 1 and figure 6). The capacity loss of Sb PAN electrode is mainly caused by the massive volume variation of Sb particles during sodiation/de-sodiation, which can lead to serious pulverization and lost contact between the conductive carbon matrix and active materials. To further increase the cycling stability, Sb nanobelts (NBs) were introduced into the asymmetric membrane structure. Indeed, the capacity retention of Sb NB PAN membrane electrode was significantly increased to 58.6% after 50 cycles, with an ICL as low as 14.3% (figure 6 and table 1). The enhanced cycling stability is due to the unique aspects of nanobelts as discussed before. Firstly, nanoscale Sb can better

accommodate the large volume expansion during charging/discharging without being seriously fractured in comparison to bulk Sb, as implied by the higher capacity retention of NB thin film electrode than powder thin film electrode (figure 6(a)). Secondly, long nanobelts allow for a greater contact area between the active materials and conductive carbon matrix, thus creating more efficient pathways for electrons to transport even though NB still experiences certain degree pulverization and volume changes during sodiation/de-sodiation. Although the cycling performance of Sb NB PAN electrode has been increased relative to Sb PAN, it is not significant enough for practical applications. Later, coating Sb NB PAN with a layer of porous carbon using the same phase inversion method was found to be an effective thrust to dramatically stabilize the electrode as evidenced by 97.5% capacity retention in 137 cycles (figure 6 and table 1). As mentioned prior, the porous carbon coating can aid in the formation of stable solid-electrolyte-interphase (SEI) on the surface of Sb NB, as well as provide another barrier to prevent the loss of active material during long term cycling. The coated membrane electrode experienced a low ICL of 13.8% and demonstrated the most outstanding high capacity, i.e. $\sim$500 mAh g^{-1} at 60 mA g^{-1} (table 1 and figure 6). Noteworthy, the dip-coated Sb NB PAN also exhibited an

a

b

c
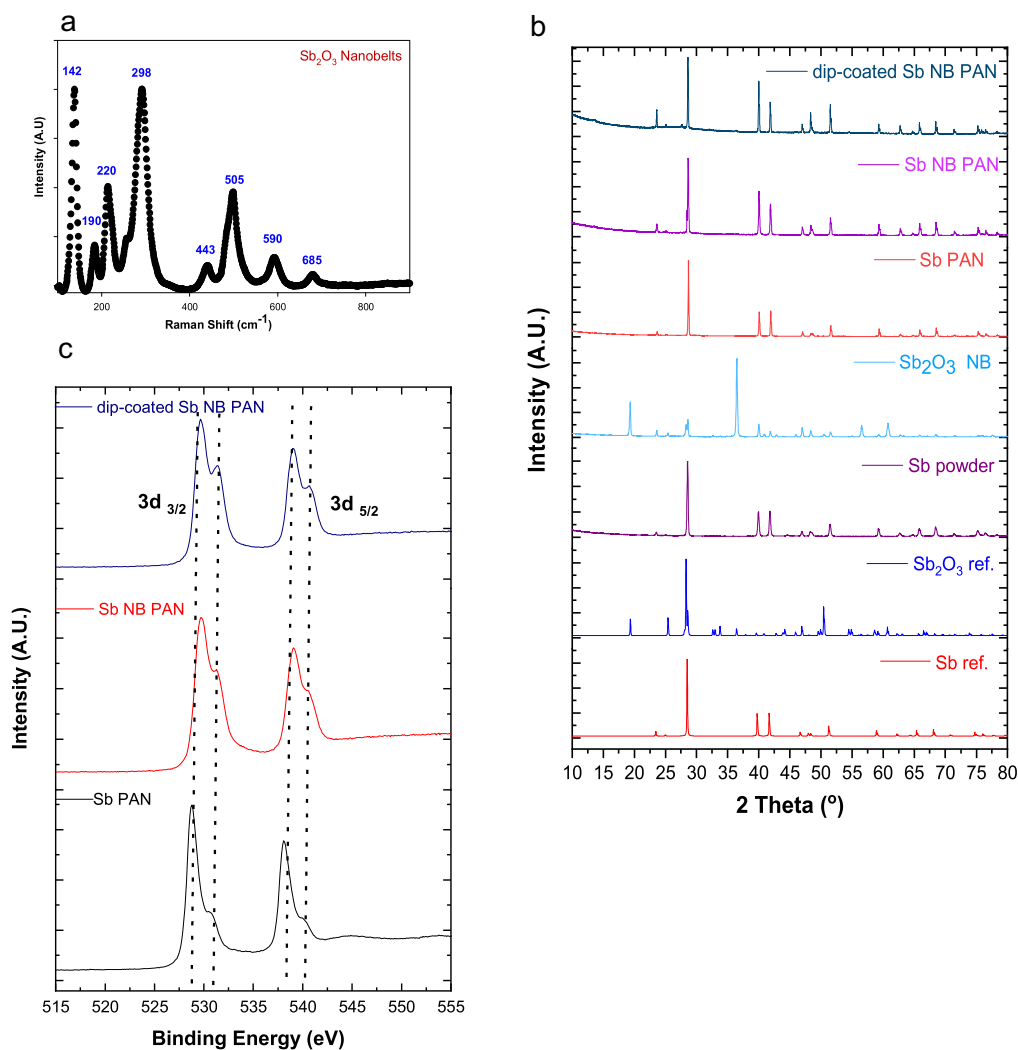

Figure 4. (a) Raman spectrum of as-synthesized antimony oxide (Sb_2O_3) nanobelts; (b) PXRD patterns of all samples: Sb powder, Sb powder asymmetric membrane, Sb_2O_3 nanobelts, Sb nanobelt asymmetric membrane, and dip-coated Sb nanobelt asymmetric membrane; (c) XPS 3d spectra of Sb powder, Sb nanobelt and dip-coated Sb nanobelt asymmetric membranes.

excellent average coulombic efficiency (CE), 99. 9% in over 100 cycles (figure 6(b)). There is negligible change in voltage profiles during the long-term cycling test (figure 6(d)), implying that the dip-coated structure can assist the creation of a very stable SEI layer while preventing any cracked materials from being lost from the electrode over the long-term cycling. Furthermore, the capacity reduction was less than 20% ($\sim$470 mAh g^{-1}) when the current density was increased from 15 to 240 mA g^{-1} (figure 6(c)), which is quite commendable for such a highly scalable fabrication method. A summary of ICL and capacity retention of three membrane samples is provided in table 1.

Cyclic voltammetry (CV) tests were performed using scanning rates of 0.1, 0.2, 0.4, and 0.8 mV s^{-1} to investigate the redox reactions and diffusivities of Na$^+$ ions in the dip-coated Sb NB PAN electrode. As seen in figure 7(a), the cathodic peak below 0.2 V at a scanning rate of 0.1 mV s^{-1} originates from the irreversible decomposition of the electrolyte during SEI formation. There also exist two redox couples at 0.65/0.93 and 0.40/0.78 V versus Na/Na$^+$ [23].

The two reduction peaks can be attributed to the 2-step alloying reactions of Sb with sodium ions, as shown below:

$$Sb + Na^+ + e^- \rightarrow NaSb \ (0.65 \ V),$$
$$NaSb + 2Na^+ + 2e^- \rightarrow Na_3Sb (0.4 \ V).$$
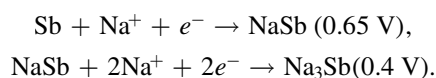
The two oxidation peaks can be assigned to the de-alloying reactions below:

$$Na_3Sb \rightarrow NaSb + 2Na^+ + 2e^- (0.78 \ V),$$
$$NaSb \rightarrow Sb + Na^+ + e^- (0.93 \ V).$$
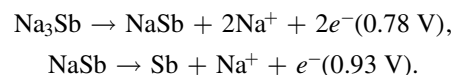
The CV results together with the voltage profiles obtained from the galvanostatic charge-discharge testing (figure 6(d)) support that the capacity of dip-coated Sb NB PAN comes from the sodiation reactions [23]. Assuming that interfacial charge transfer is fast and ionic diffusion is the rate limiting step, the diffusion coefficient of Na$^+$ in dip-coated Sb NB PAN membrane electrode can be calculated using the plots shown in figure 7(b) and Randles-Sevcik equation listed below [24, 25]:

$$I_{pc} = (2.69 \ \times \ 10^5) n^{1.5} A D_{Na+}^{0.5} C_{Na+} v^{0.5}, \tag{1}$$
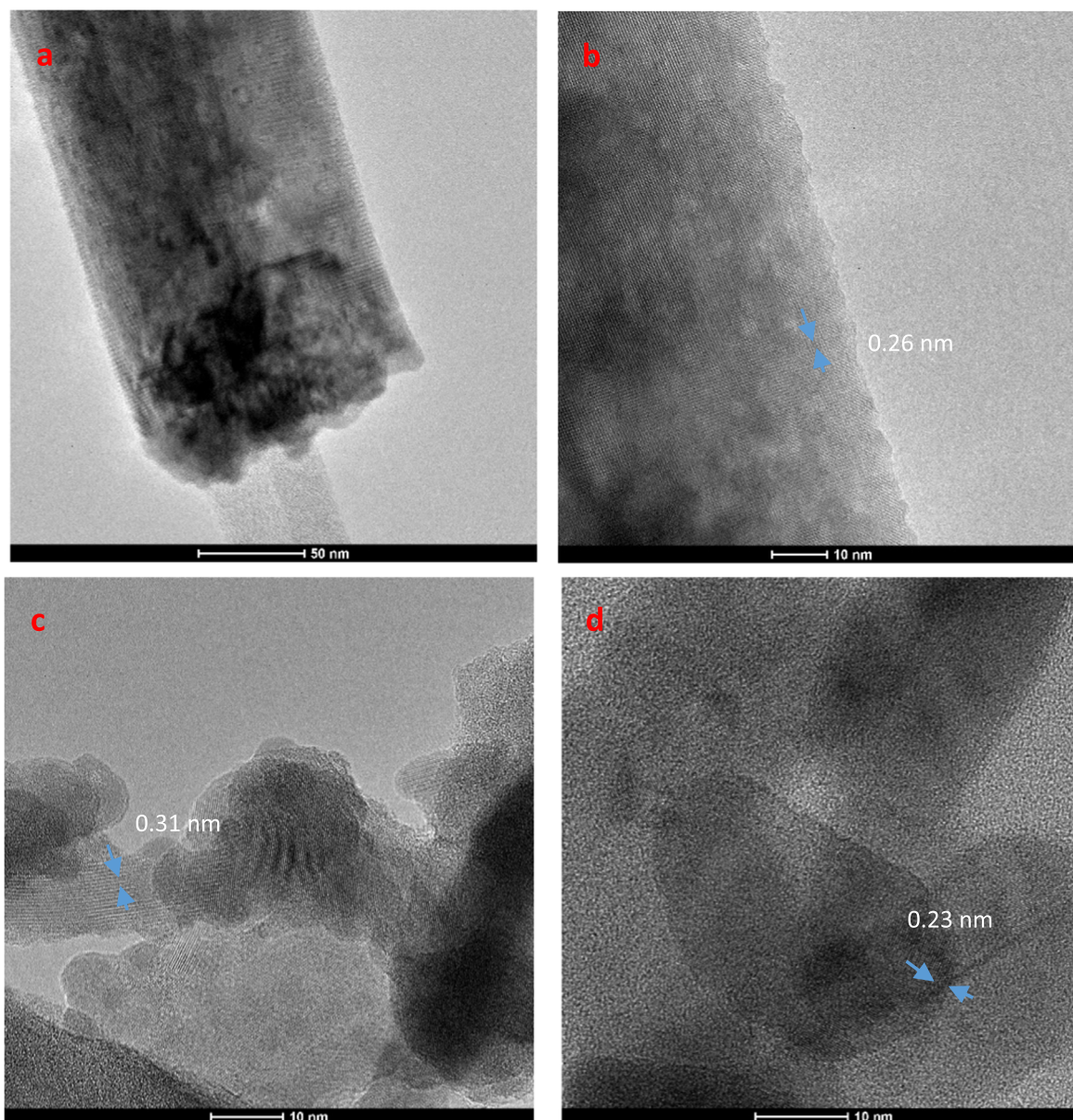
Figure 5. High resolution TEM images: (a) and (b) as-synthesized Sb_2O_3 NB; (c) Sb NBs in Sb NB PAN; (d) Sb NBs in dip-coated Sb NB PAN. Notes: scale bars in (a)–(d) are 50, 10, 10 and 10 nm, respectively.

where I_{pc} is the cathodic peak current in amps corresponding to Na^+ insertion, n is the number of charges transferred, A is the nominal surface area of the membrane electrode, C_{Na+} is the bulk concentration of Na^+ in mol cm^{-3}, and v represents CV scan rate in V s^{-1}. D_{Na+}, the nominal diffusivity of Na^+ in dip-coated Sb NB PAN membrane electrode was calculated to be 1.6×10^{-3} cm^2 s^{-1} using the first cathodic peak ($n = 1$). If the nominal surface area is replaced by the surface area of Sb_2O_3 NBs as determined by using a surface area and porosity analyzer ($\sim$2.2 m^2 g^{-1}; see S4), the diffusivity was found to be 1.0×10^{-5} cm^2 s^{-1}. The outstanding diffusivities can be attributed to the usage of NBs that have a large specific surface area as compared to the bulk counterpart, also being consistent with the reports from Manthiram *et al* and many others [26–28].

EIS spectroscopy was utilized to measure the resistances of ohmic contact, electrolyte, charge transfer and SEI layer on the dip-coated Sb NB PAN membrane electrode in a fully de-sodiated state (S5). Nyquist plots of the electrode at different cycles indicate there is no significant change in the ohmic internal resistance during the long-term cycling process (5.2 versus 3.4 ohm for 1st and 100th cycles, respectively). R_{ct} decreases from 338 to 35 ohm in the first 100 cycles since the electrode surface has been fully wetted by the electrolyte and thus become more accessible to sodium ions; whereas R_{SEI} has been gradually increased, duo to the formation of new SEI layers as the result of the structural change of NBs after repeated sodiation/de-sodiation. Nyquist plots were measured four times each after 1st and 100th cycles, and the four repeating measurements are nearly identical to each other as shown in S6.
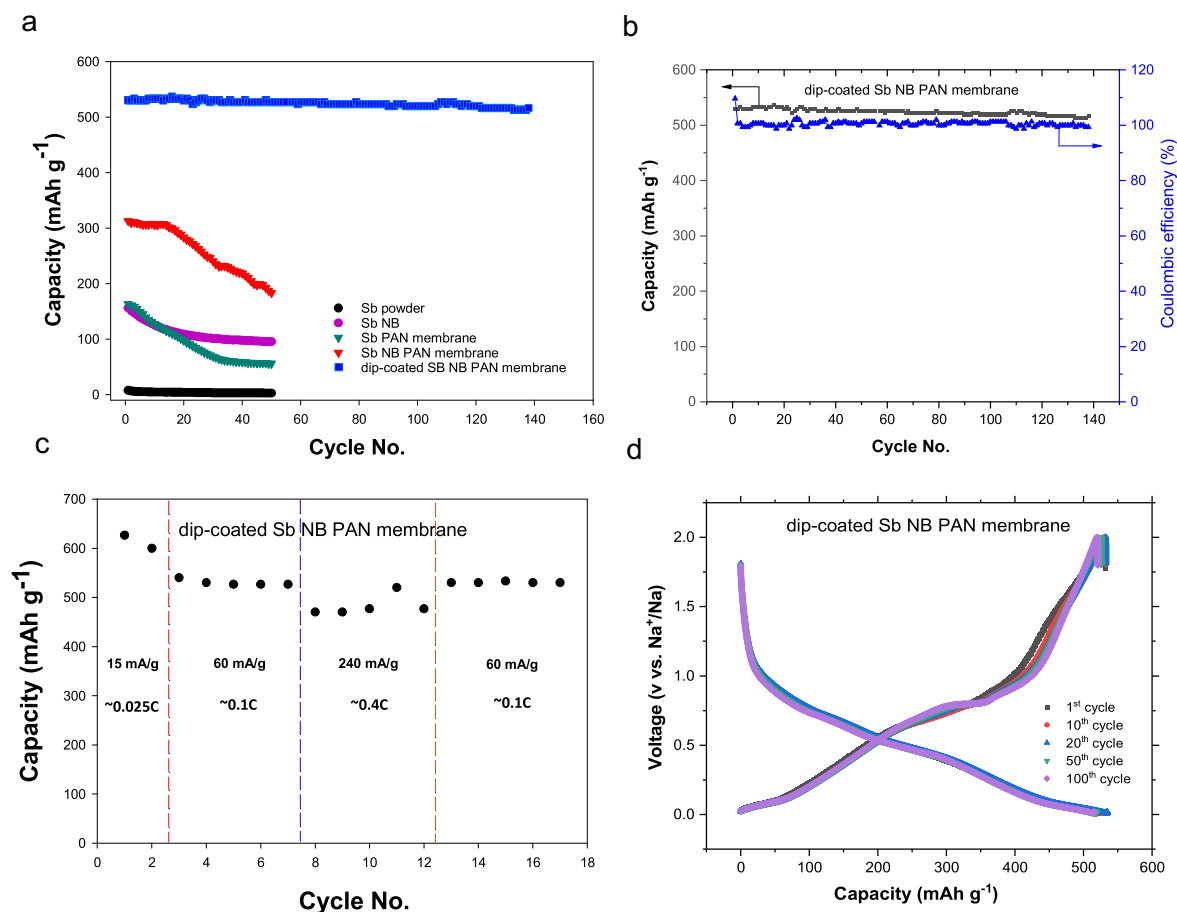
Figure 6. (a) Cycling performance of Sb PAN, Sb NB PAN, dip-coated Sb NB PAN membrane electrodes and two controls: Sb *powder and* Sb NB thin film electrodes; (b)–(d) cycling performance and coulombic efficiency, rate tests, voltage profiles of dip-coated Sb NB PAN electrode, respectively.
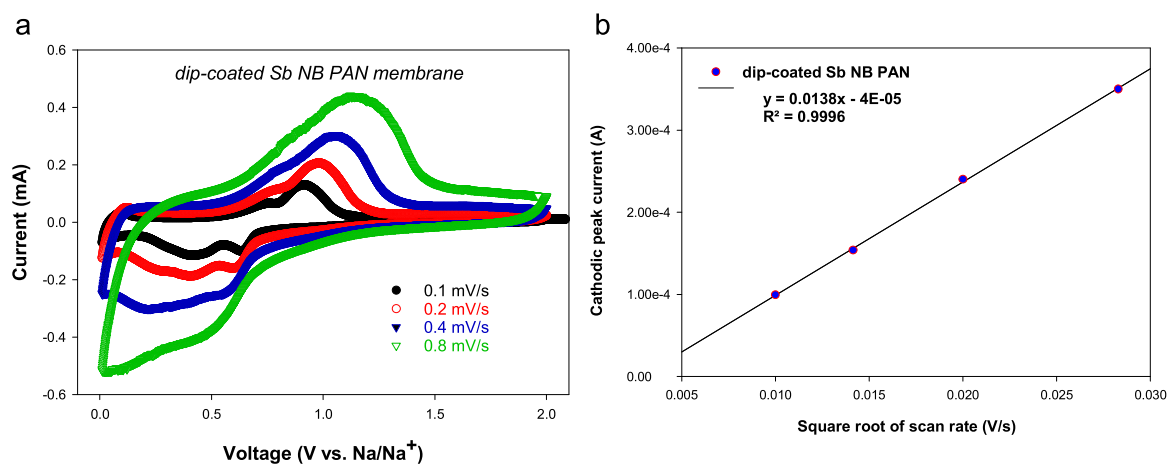
Figure 7. (a) Cyclic voltammograms (CV) of dip-coated Sb NB PAN at different scanning rates; (b) cathodic peak current versus square root of scan rate plot used to calculate the diffusivity of Na$^+$ in dip-coated Sb NB PAN electrode.

Table 1. Summary of the initial capacity loss (ICL) and capacity retention for Sb PAN, Sb NB PAN and dip-coated Sb NB PAN membranes.

	Sb PAN	Sb NB PAN	Dip-coated Sb NB PAN
Initial Capacity Loss (ICL)	25.5%	14.3%	13.8%
Capacity retention	34.1% (50 cycles)	58.6% (50 cycles)	97.5% (137 cycles)

4. Conclusion

A scalable, low cost, efficient, novel method to prepare high-capacity anode materials for high-capacity SIBs has been demonstrated as accompanied by systematic characterization and various electrochemical evaluation. Asymmetric membrane structure can stabilize Sb-based SIB alloy anodes as compared to traditional thin film structure. Also, the electrochemical performance of the membrane electrode made from antimony nanobelts is better than that of the electrode containing micron-sized Sb particles, owing to the unique nanostructure that can create more contact points between conductive additives and active materials, allow for more tolerable volume expansion, as well as provide much-shortened diffusion length. Creating an additional layer of porous carbon on the surface of the Sb nanobelt asymmetric membrane further aids in the cycling performance of the electrodes with a capacity retention of 97.5% after 137 cycles at a capacity above 500 mAh g^{-1}. The carbon coating also facilitates rapid electron transport and results in excellent rate performance as evident by less than 20% capacity loss when the current density is increased by more than 10 folds. The reported electrode structure bears a great potential once being optimized with appropriate membrane thickness, concentration of Sb nanobelts, carbon coating thickness, phase inversion temperature, etc. In the future, other types of nanobelts are going to be introduced into asymmetric membranes for lithium and sodium ion batteries, such as tin and silicon nanobelts. Additionally, different conductive fillers will replace carbon black to investigate their effect on electrochemical properties, including graphene, graphene oxide and various carbon nanotubes (1D). Furthermore, 3-electrode cells are going to be employed to collect EIS spectra.

Data availability statement

All data that support the findings of this study are included within the article (and any supplementary files).

ORCID iDs

Congrui Jin ⬤ https://orcid.org/0000-0003-0606-5318
Ji Wu ⬤ https://orcid.org/0000-0002-0069-3260

References

[1] Armand M *et al* 2020 Lithium-ion batteries—current state of the art and anticipated developments *J. Power Sources* **479** 228708

[2] Blomgren G E 2016 The development and future of lithium ion batteries *J. Electrochem. Soc.* **164** A5019–25

[3] Ritchie A and Howard W 2006 Recent developments and likely advances in lithium-ion batteries *J. Power Sources* **162** 809–12

[4] Aral H and Vecchio-Sadus A 2008 Toxicity of lithium to humans and the environment—A literature review *Ecotoxicology Environ. Saf.* **70** 349–56

[5] Flexer V, Baspineiro C F and Galli C I 2018 Lithium recovery from brines: a vital raw material for green energies with a potential environmental impact in its mining and processing *Sci. Total Environ.* **639** 1188–204

[6] Hwang J-Y, Myung S-T and Sun Y-K 2017 Sodium-ion batteries: present and future *Chem. Soc. Rev.* **46** 3529–614

[7] Abraham K M 2020 How comparable are sodium-ion batteries to lithium-ion counterparts? *ACS Energy Lett.* **5** 3544–7

[8] Yabuuchi N, Kubota K, Dahbi M and Komaba S 2014 Research development on sodium-ion batteries *Chem. Rev.* **114** 11636–82

[9] Hou H, Qiu X, Wei W, Zhang Y and Ji X 2017 Carbon anode materials for advanced sodium-ion batteries *Adv. Energy Mater.* **7** 1602898

[10] Jing W T, Yang cc and Jiang Q 2020 Recent progress on metallic Sn- and Sb-based anodes for sodium-ion batteries *J. Mater. Chem. A* **8** 2913–33

[11] Liu Z, Yu X-Y, Lou X W and Paik U 2016 Sb@C coaxial nanotubes as a superior long-life and high-rate anode for sodium ion batteries *Energy Environ. Sci.* **9** 2314–8

[12] Wu L, Hu X, Qian J, Pei F, Wu F, Mao R, Ai X, Yang H and Cao Y 2014 Sb–C nanofibers with long cycle life as an anode material for high-performance sodium-ion batteries *Energy Environ. Sci.* **7** 323–8

[13] Liang L, Xu Y, Wang C, Wen L, Fang Y, Mi Y, Zhou M, Zhao H and Lei Y 2015 Large-scale highly ordered Sb nanorod array anodes with high capacity and rate capability for sodium-ion batteries *Energy Environ. Sci.* **8** 2954–62

[14] Wu L, Pei F, Mao R, Wu F, Wu Y, Qian J, Cao Y, Ai X and Yang H 2013 SiC–Sb–C nanocomposites as high-capacity and cycling-stable anode for sodium-ion batteries *Electrochim. Acta* **87** 41–5

[15] Zhao Y and Manthiram A 2015 High-capacity, high-rate Bi–Sb alloy anodes for lithium-ion and sodium-ion batteries *Chem. Mater.* **27** 3096–101

[16] Byrd I and Wu J 2016 Asymmetric membranes containing micron-size silicon for high performance lithium ion battery anode *Electrochim. Acta* **213** 46–54

[17] Wu J, Anderson C, Beaupre P, Xu S, Jin C and Sharma A 2019 Co-axial fibrous silicon asymmetric membranes for high-capacity lithium-ion battery anode *J. Appl. Electrochem.* **49** 1013–25

[18] Wu J, Byrd I, Jin C, Li J, Chen H, Camp T, Bujol R, Sharma A and Zhang H 2017 Reinvigorating reverse-osmosis membrane technology to stabilize the V2O5 lithium-ion battery cathode *Chem. Electro. Chem.* **4** 1181–9

[19] Wu J, Chen H, Byrd I, Lovelace S and Jin C 2016 Fabrication of SnO₂ asymmetric membranes for high performance

lithium battery anode *ACS Appl. Mater. Interfaces* **8** 13946–56

[20] Wu J, Chen H and Padgett C 2016 Silicon asymmetric membranes for efficient lithium storage: a scalable method *Energy Technol.* **4** 502–9

[21] Wu J, Jin C, Larson E and Williams L 2020 Etching asymmetric germanium membranes with hydrogen peroxide for high-capacity lithium-ion battery anodes *Phys. Status Solidi (a)* **217** 1900963

[22] Deng Z, Chen D, Tang F, Ren J and Muscat A J 2009 Synthesis and purple-blue emission of antimony trioxide single-crystalline nanobelts with elliptical cross section *Nano Res.* **2** 151–60

[23] Liu M, Yang Z, Shen Y, Guo S, Zhang J, Ai X, Yang H and Qian J 2021 Chemically presodiated Sb with a fluoride-rich interphase as a cycle-stable anode for high-energy sodium ion batteries *J. Mater. Chem. A* **9** 5639–47

[24] Ngamchuea K, Eloul S, Tschulik K and Compton R G 2014 Planar diffusion to macro disc electrodes—what electrode size is required for the Cottrell and Randles-Sevcik equations to apply quantitatively? *J. Solid State Electrochem.* **18** 3251–7

[25] Yang T, Niu X, Qian T, Shen X, Zhou J, Xu N and Yan C 2016 Half and full sodium-ion batteries based on maize with high-loading density and long-cycle life *Nanoscale* **8** 15497–504

[26] Allcorn E, Kim S O and Manthiram A 2015 Lithium diffusivity in antimony-based intermetallic and FeSb-TiC composite anodes as measured by GITT *Phys. Chem. Chem. Phys. : PCCP* **17** 28837–43

[27] Ding N, Xu J, Yao Y X, Wegner G, Fang X, Chen C H and Lieberwirth I 2009 Determination of the diffusion coefficient of lithium ions in nano-Si *Solid State Ionics* **180** 222–5

[28] Wang Z, Su Q, Deng H, He W, Lin J and Fu Y Q 2014 Modelling and simulation of electron-rich effect on Li diffusion in group IVA elements (Si, Ge and Sn) for Li ion batteries *J. Mater. Chem. A* **2** 13976–82